MNRAS **000**, ??–11 (2016) Preprint 10 August 2016 Compiled using MNRAS LATEX style file v3.0

The Luminosity and Stellar Mass Functions of Red W1-W2 Galaxies

J. A. O'Connor,[1⋆] J. L. Rosenberg[1] S. Satyapal[1] N.J. Secrest[1,2]
[1] *Department of Physics and Astronomy, George Mason University, Fairfax, VA 22030*
[2] *United States Naval Observatory*

arXiv:1608.02648v1 [astro-ph.GA] 8 Aug 2016

Accepted 2016 August 05. Recieved 2016 July 24; in original form 2015 December 16

ABSTRACT

We present a study of nearby galaxies as a function of their [3.4]-[4.6] colour. Galaxies that are red in their [3.4]-[4.6] colour contain heated dust and the reddest systems ([3.4]-[4.6] > 0.5) are classified as AGN by some selection criteria. The sample discussed here includes nearby galaxies selected from the Sloan Digital Sky Survey (SDSS) that are also in the Wide-field Infrared Survey Explorer (WISE) catalogue. We calculate the number density of galaxies, in the form of the luminosity and mass functions, using the V/Vmax method and a Stepwise Maximum Likelihood method that has been modified to account for the additional colour selection. The reddest galaxies which have [3.4]-[4.6] > 0.8 and are sometimes classified as AGN by their colour, make up 0.2% of nearby galaxies. However, the reddest galaxies are a rising fraction of the low mass galaxy population. Identifying the lowest mass ($M < 10^8 M_\odot$) red ([3.4]-[4.6] > 0.8) galaxies as AGN is surprising given that none are optical AGN or composites, in contrast with their more massive ($M > 10^{10} M_\odot$) red galaxy counterparts that are dominated by optical AGN and composites (86.4%). We also show that these low mass red galaxies are associated with higher specific star formation rates than their bluer counterparts. While the properties of this relatively rare segment of nearby low-mass galaxies are intriguing, particularly if they are associated with AGN activity, there is not yet enough evidence to determine whether it is AGN or unusual star formation that is driving red colours in these systems.

Key words: galaxies: luminosity function, mass function; infrared: galaxies; ISM: dust, extinction

1 INTRODUCTION

Infrared (IR) colours of galaxies observed by the *Wide-Field Infrared Survey Explorer* (WISE) provide a probe of hot dust emission (Jarrett et al. 2011; Donley et al. 2012; Mateos et al. 2012; Stern et al. 2012). Active galactic nuclei (AGN) activity and star formation are the dominant processes that heat the dust and thus galaxies with very red [3.4]-[4.6] (W1 - W2) colours provide a probe of the most extreme interstellar medium environments. The luminosity and mass functions of galaxies with red W1 - W2 colours measure the prevalence of these extreme environments in the local universe.

AGNs have a hard radiation field that, in dusty systems, is absorbed and re-radiated in the infrared. The spectral energy distributions (SEDs) of AGNs are predicted to display power law slopes ($f_\nu \propto \nu^\alpha$ with $\alpha < -0.5$) (Alonso-Herrero et al. 2006) in the infrared producing red colours in W1 - W2 (or equivalently the [3.6] - [4.5] Spitzer bands; Richards et al. 2006; Polletta et al. 2007; Assef et al. 2010). Observationally Yan et al. (2013) have shown that QSOs and some Seyfert galaxies selected from the *Sloan Digital Sky Survey* (SDSS) have redder W1 - W2 colours than star-forming galaxies. Jarrett et al. (2011), Stern et al. (2012), and Mateos et al. (2012) have created AGN selection criteria based primarily on a galaxy's W1 - W2 colour, though Jarrett et al. (2011) and Mateos et al. (2012) also make use of W2 - W3 ([4.6] - [12]) colour in their diagnostics. For W1 - W2 > 0.8, 95% of the galaxies in the COSMOS field are AGNs (Stern et al. 2012). This selection technique is particularly sensitive to heavily obscured or Compton-Thick AGN, which may not be visible in optical or X-ray wavelengths (Goulding et al. 2011; Assef et al. 2013; Mateos et al. 2013; Rovilos et al. 2014; Stern et al. 2014).

⋆ E-mail: joconno5@gmu.edu

© 2016 The Authors

While the aforementioned work shows that AGNs can have extreme MIR colours, extreme star formation may also heat the dust in galaxies and lead to excess emission in the longer wavlelengths of *WISE* (Schaerer & de Koter 1997; Ranalli et al. 2003; Charmandaris et al. 2008). Longer mid-infrared wavelengths such as MIPS 24μm(Kennicutt 1998), W3 (12μm) and W4 (22μm) (Jarrett et al. 2013; Lee et al. 2013), and IRAC 4 (8μm) (Calzetti et al. 2007; Bendo et al. 2008) are used for measurments of star formation rates for this reason.

Satyapal et al. (2014) found that the fraction of galaxies in the local universe with extreme mid-infrared colours is higher in low mass galaxies than at high stellar masses. It is unclear why the number of red low mass galaxies is so large and whether the dominant cause of their dust heating is extreme star formation or AGN activity. We examine the number density of these systems and their contribution to the overall galaxy population and properties from the optical spectra which may explain the nature of their nuclear activity. Throughout this paper we will use H_0=70 km s^{-1} Mpc^{-1}, Ω_m=0.3 and Ω_Λ=0.7.

2 SAMPLE SELECTION

Our galaxy sample is selected from the Sloan Digital Sky Survey (SDSS) data release 7 (DR7) catalogue (Abazajian et al. 2009) and includes all spectroscopic objects in the Legacy area with SpecPhoto.specClass=2 (Galaxies) or SpecPhoto.specClass=3 (QSOs), 0.005 $\leq$ z $\leq$ 0.1 and the Petrosian r-band magnitude, corrected for Galactic extinction (Schlegel et al. 1998), 14.0 $\leq r \leq$ 17.77. The SDSS Legacy Survey is a spectroscopic and photometric optical survey covering over 8000 deg^{-2} on the sky. The faint magnitude limit, r=17.77, represents the completeness limit of the DR7 spectroscopic sample (Strauss et al. 2002). On the other hand, galaxies with $r < 14$ may have unreliable photometry due to shredding (Strauss et al. 2002). The resulting sample contains ≈315,000 galaxies.

The SDSS sample was matched, within 3″, with galaxies in the AllWISE Catalogue (Wright et al. 2010; Mainzer et al. 2011; Cutri et al. 2013)[1] that have S/N > 5.0 at both 3.4 μm (W1) and 4.6 μm (W2). The angular resolution of WISE is approximately 6″ in the W1 and W2 bands. Out of the SDSS galaxies with WISE matches (315251 galaxies or 99.7% of the SDSS sample), 6837 (2.2%) have two WISE matches and 67 (0.002%) have 3 WISE matches. In the infrared and optical images, these multiple matches appear to be single galaxies that WISE identifies two or three times, generally with the WISE position straddling the centre of the galaxy, although it is not clear why in these limited cases WISE separated the galaxies into two or three infrared sources. For these systems the photometry for the source closest to the SDSS spectrum was used. Only 0.8% of galaxies with W1 -W2 > 0.3 have multiple WISE sources where the closest source to the SDSS spectrum is not also the brightest. For galaxies that are resolved in WISE, the difference in resolution can cause an underestimation of the W1 band profile flux. Therefore, in the case of sources with w1rchi2 > 2 we use 11″ aperture photometry in the W1 and W2 bands instead of the profile magnitudes. 1.4% of randomly selected positions within the SDSS footprint (for a selection of 4400 sources) have a match in the ALLWISE catalogue within 3″ that has W1 and W2 S/N $\geq$ 5.0 so almost all of the matches are expected to be legitimate.

Stellar masses for the galaxies were obtained from the NYU-VAGC (Blanton et al. 2005b; Blanton & Roweis 2007)[2] which were derived from principal component analysis fits to stellar templates. Emission line fluxes used to calculate star formation rates (Brinchmann et al. 2004) and metallicities (Tremonti et al. 2004) were obtained from the MPA-JHU catalogue[3]. This catalogue contains line fluxes corrected for stellar absorption using the Bruzual & Charlot (2003) stellar population templates.

3 METHODS

We compute the luminosity and stellar mass functions for the galaxies in our sample using the $1/V_{Max}$ (Schmidt 1968) method and a modified form of the stepwise maximum likelihood method (SWML; Efstathiou et al. 1988) which are not susceptible to the same biases and therefore provide a check on the results.

The $1/V_{Max}$ method is used to calculate the number of galaxies per luminosity, absolute magnitude, or stellar mass bin weighted according to the volume in which each galaxy could have been detected. For each galaxy in the sample there are both a minimum and a maximum distance at which it would be included in the V_{max} volume. The lower bound to the distance is the larger value of 21 Mpc (defined by the z=0.005 minimum redshift for the sample) or the minimum distance at which the galaxy would be included in the sample based on the bright limit $r > 14.0$ for galaxies in the sample. The maximum comoving distance is 418 Mpc (defined by the redshift limit of the sample z=0.1) or the maximum distance based on the faint limit, $r < 17.77$ for galaxies in the sample.

The $1/V_{Max}$ method has the advantage of being a relatively simple calculation with built-in normalization, but it relies on the assumption that galaxies are distributed homogeneously throughout the survey volume. The value of $< \frac{V}{V_{Max}} >$ for this sample is 0.4877±0.0005 where a value of 0.5 indicates an evenly distributed sample. The CfA Great Wall (Geller & Huchra 1989) and the Coma Cluster (Harrison et al. 2010) contribute to an excess of galaxies at 0.02 < z < 0.04 while the SDSS Great Wall (Gott et al. 2005) is responsible for an excess near z≈0.08. To mitigate the impact of large-scale seen in Figure 1 structure on the number density the $1/V_{Max}$ values have been corrected by a factor of n, the number of galaxies in the SDSS sample that are within a given redshift range divided by the number of galaxies expected to fall in that range if they are distributed according to the Blanton et al. (2005a) r-band luminosity function.

[1] http://irsa.ipac.caltech.edu/Missions/wise.html

[2] http://sdss.physics.nyu.edu/vagc/

[3] http://home.strw.leidenuniv.nl/ jarle/SDSS/

3.1 Modified Stepwise Maximum Likelihood Method

The stepwise maximum likelihood method (SWML) (Efstathiou et al. 1988) for measuring the luminosity and mass functions of galaxies has the advantage of being insensitive to cosmic variance within the survey volume. For the purposes of this work we modify the standard SWML technique to account for a galaxy selection (W1-W2 colour) that does not affect the detectability of the galaxy.

In the standard formulation of the SWML method, the number density of galaxies in a given bin of luminosity (or absolute magnitude or stellar mass) is given by:

$$\phi_k = N_k \left[\sum_{i=1}^{N_{gal}} \frac{H_{ki}\Delta M_k}{\sum_{n=1}^{N_M} \phi_n \Delta M_k H_{ni}} \right]^{-1} \quad (1)$$

We derive a normalization for the SWML points by assuming that the total galaxy density within the luminosity range sampled will match that calculated using the $1/V_{Max}$ method. N_k is the number of galaxies in magnitude bin k, H_{ki} is the fraction of bin k in which galaxy i is detectable, N_{gal} and N_M are the number of galaxies in the sample and number of absolute magnitude bins, respectively. Equation 1 is iterated upon until all ϕ_k values change by less than 1% between successive iterations. Equation 2 shows the comparable expression for the mass function (Loveday 2000). In this case the expression is two-dimensional. N_{jk} is the number of galaxies in absolute magnitude bin j and stellar mass bin k and H_{ji} and H_{ki} are the fraction of magnitude bin j and stellar mass bin k in which galaxy i could have been detected.

$$\phi_{jk} = N_{jk} \left[\sum_{i=1}^{N_{gal}} \frac{H_{ji}H_{ki}\Delta M_j \Delta M_{*k}}{\sum_{m=1}^{N_M}\sum_{n=1}^{N_{M*}} \phi_{mn} H_{mi} H_{ni} \Delta M_m \Delta M_{*n}} \right]^{-1} \quad (2)$$

Because the only limiting quantity is the r-band apparent magnitude, Equation 2 can be simplified by assuming that if galaxy i is detectable in magnitude bin j ($H_{ji} > 0$) then $H_{ki} = 1$:

$$\phi_{jk} = N_{jk} \left[\sum_{i=1}^{N_{gal}} \frac{H_{ji}\Delta M_j \Delta M_{*k}}{\sum_{m=1}^{N_M}\sum_{n=1}^{N_{M*}} \phi_{mn} H_{mi} \Delta M_m \Delta M_{*n}} \right]^{-1} \quad (3)$$

Equation 3 is then summed over magnitude bins j in order to calculate values of ϕ_k (Loveday 2000).

$\phi_{k,x}$ is the number density of galaxies in a given stellar mass or magnitude bin k and W1-W2 colour bin x. This number density is determined by multiplying the number density of the full sample by the probability of a galaxy in bin k falling in colour range x:

$$\phi_{k,x} = \phi_k \frac{N_{k,x}}{N_k} \quad (4)$$

The 1-sigma uncertainties for the full sample are calculated from the information matrix (Efstathiou et al. 1988). The inverse of this matrix contains the variance in ϕ_k. Uncertainties for subsamples are calculated by adding the uncertainties in ϕ_k in quaderature with the uncertainties from Equation 4.

4 RESULTS

Figures 2 and 3 show the luminosity and stellar mass functions for galaxies in our sample (black circles) as well as for subsamples with infrared colours W1 - W2 $\geq$ 0.3 (blue stars), W1 - W2 $\geq$ 0.5 (green triangles) and W1 - W2 $\geq$ 0.8 (red squares). In order to distinguish values determined using the $1/V_{Max}$ method (filled points, solid lines) from those determines using the SWML method (open points, dotted lines), the SWML points have all been multiplied by 1.5. Without this artificial separation, the results of the two methods lie on top of one another. Solid lines represent the best fit Schechter functions to the $1/V_{Max}$ points. The details of the functions will be discussed later in this

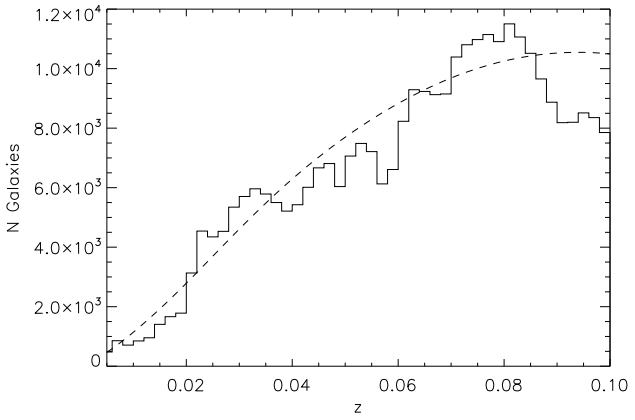

Figure 1. The cumulative number of galaxies as a function of redshift in this sample (solid histogram). The dashed line shows the cumulative number of galaxies expected as a function of redshift assuming the SDSS DR2 luminosity function (Blanton et al. 2005a).

section. The $1/V_{Max}$ and SWML methods yield luminosity and stellar mass functions with similar shapes indicating that the structure is not due to cosmic variance within the survey volume.

The $1/V_{Max}$ and SWML functions are in good agreement with the yellow points in Figure 2 which show the SDSS DR6 r-band luminosity function from Montero-Dorta & Prada (2009). Figure 3 shows the total stellar mass function (black) plotted alongside the mass function results from Baldry et al. (2012) (yellow). The downturn at the low mass end of the stellar mass function is due to surface brightness incompleteness in the SDSS sample and is also seen in Baldry et al. (2008) and Baldry et al. (2012). Due to this incompleteness, all points below $\log(M/M_{\odot})$=8 and M_r=-16.5 (dashed lines in Figures 2 and 3) are treated as lower limits and not used to determine the Schechter function fits.

Schecter functions with two characteristic number densities (ϕ_1^*, ϕ_2^*), one characteristic magnitude or stellar mass (M^*) and two power law slopes (α_1, α_2) were fit to the points brighter than the surface brightness incompleteness limit. This double Schecter form is the same one used in Blanton et al. (2005a) and Baldry et al. (2012). Parameters of the best fit functions are listed in Tables 1 and 2.

The Schecter functions for galaxies with W1 - W2 $\geq$ 0.3, 0.5, and 0.8 have two components such that the luminosity functions "dip" at intermediate luminosities. This dip can be seen in Figure 2 and in the values for α_1 (the power law slope of the high luminosity population) α_1=0.463, α_1=0.473 and α_1=0.217 (Table 1). This slope is in the opposite direction of the one measured for the full sample, α_1=-0.244. The mass functions in Figure 3 and Table 2 show a similar pattern. For the full stellar mass function, α_1=-0.557 indicating a smooth transition between the high and low mass galaxy populations. However, the values of α_1 for W1 - W2 $\geq$ 0.3, 0.5 and 0.8 are much higher (α_1=-0.137, 0.423, 0.479). This is evident as a decrease in the number density from the high to intermediate stellar mass population of red galaxies in Figure 3.

In addition to this dip, the power law slopes of the red low mass/low luminosity galaxies are much steeper than those of the total stellar mass and luminosity functions. For the total stellar mass function, α_2=-1.524. This becomes steeper (more negative) for redder galaxy populations. The values of α_2 decrease from -1.804 at W1 - W2 $\geq$ 0.3 to -1.892 at W1 - W2 $\geq$ 0.5 and -1.487 for galaxies with W1 - W2 $\geq$ 0.8. The faint end slopes of the luminosity functions display a similar trend with values decreasing from α_2=-1.438 for the full sample to α_2=-1.973 for galaxies with W1-W2$\geq$0.8.

The functional forms of the galaxy luminosity and stellar mass functions are bimodal for W1 - W2 $\geq$ 0.3. The low mass components come close to dominating by number density. Galaxies with M_r > -18 comprise 46.7% of the total number density (comparing to galaxies with -24 < M_r < -16.5). For galaxies with W1 - W2 $\geq$ 0.5 almost 52% of galaxies have M_r > -18. However, red galaxies do not make up a large fraction of the total number density. Galaxies with W1 - W2 $\geq$ 0.3, 0.5 and 0.8 only account for 5.6, 0.7 and 0.2% of the number density of galaxies. Low mass galaxies ($\log(M/M_{\odot})$ <9) make up 69.4% of galaxies (8 <$\log(M/M_{\odot})$ < 12) with W1 - W2 $\geq$ 0.3, 62.9% with W1 - W2 $\geq$ 0.5 and 29.9% with W1 - W2 $\geq$ 0.8.

Increasing the S/N selection threshold from 5.0 to 10.0 in the W1 and W2 bands for inclusion in our galaxy sample results in a decrease in the number density of galaxies at low masses and luminosities but due to the compact nature of the red WISE sources (discussed further in Section 5.1) this mainly affects the samples with W1 - W2 < 0.5. In addition, using the IRAF task ELLIPSE to calculate the photometry for 60 galaxies spanning a range of W1-W2 colour, S/N and angular size and comparing them to the values in the ALLWISE catalogue shows no significant trends in the catalogue colours as a function of any of these properties. The average offset between the W1-W2 colours from the AllWISE catalogue and the IRAF photometry is 0.005 mag. In short, there is no evidence that the red colours of these galaxies are artifacts of poor photometry.

4.1 Optical Nuclear Activity Classification

The classifications of galaxies in Figure 4 are based on optical emission line ratios with divisions between star-forming, composite, and AGN regions from Kewley et al. (2001) and Kauffmann et al. (2003). The AGN classification includes both broad and narrow line systems. Galaxies are unclassified if they have S/N<3 for the Hα, Hβ, [O III 5007] or [N II 6584] lines. As in Figure 3, points below $10^8 M_{\odot}$ are effected by surface brightness incompleteness and are, therefore, lower limits.

Figure 4 shows that optically classified AGNs are found almost exclusively at high stellar masses, in agreement with Kauffmann et al. (2003). However, the majority of high stellar mass galaxies are optically unclassified because they lack strong emission lines. Similarly, nearly all massive galaxies with W1-W2 > 0.5 and W1 - W2 > 0.8 are strongly dominated by AGNs in agreement with both the optically selected AGN samples of Kauffmann et al. (2003) and the X-ray and IR-selected samples of Xue et al. (2010). The fraction of optically classified AGNs drops rapidly towards lower masses. For all infrared colours, the optical emission lines of low mass galaxies are dominated by star formation, consistent with the optical emission line studies of Kewley et al. (2006).

4.2 The Impact of Metallicity and Specific Star Formation Rates on Galaxy Colour

Figure 5 shows the average specific star formation rates (sSFRs), Sérsic indices (n) and metallicities for galaxies with W1 - W2 < 0.3 in bins of stellar mass (black points). Note that the black points in each panel are the same. The red points show the average sSFRs, Sérsic indices and metallicities for galaxies with W1 - W2 $\geq$ 0.3 (left), W1 - W2 $\geq$ 0.5 (middle), and W1 - W2 $\geq$ 0.8 (right). Specific star formation rates and metallicities are drawn from the MPA-JHU catalogue (Brinchmann et al. 2004; Tremonti et al. 2004). Sérsic indices come from Table 3 of Simard et al. (2011). The sSFRs are only included for galaxies with S/N $\geq$ 3 in Hα and metallicities are only included for galaxies with S/N $\geq$ 3 in Hα, Hβ, [O III 5007] and [O III 3727]. The values for each galaxy are weighted by $1/V_{Max}$ to account for its detectability. The errors are the standard deviation in the bin divided by the square root of the number of galaxies. It should be

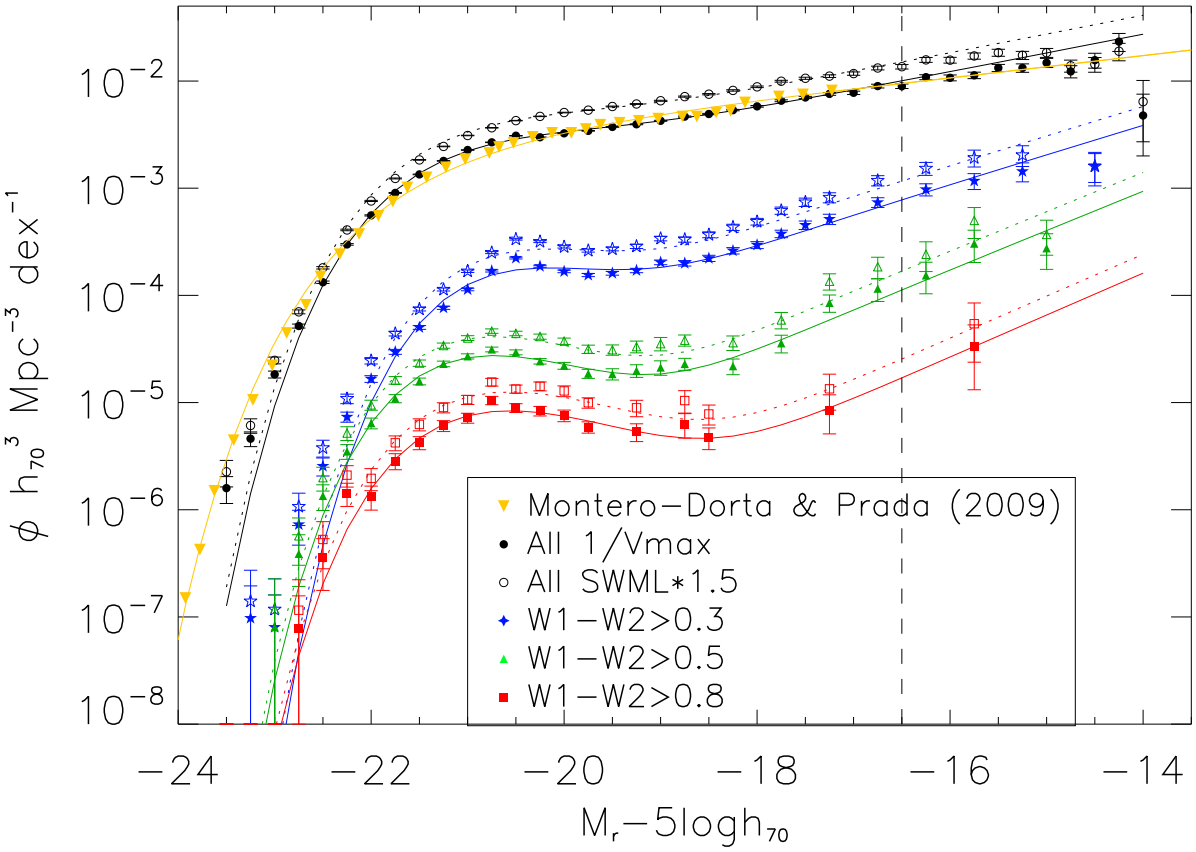

Figure 2. The number density of galaxies in our full sample (black circles) and W1 - W2 colour subsamples (W1 - W2 $\geq$ 0.3, blue stars; W1 - W2$\geq$0.5, green triangles; W1 - W2$\geq$0.8, red squares) as a function of r-band absolute magnitude. The figure shows values calculated using the $1/V_{Max}$ (filled points) and the SWML (open points). SWML values and errors are multiplied by 1.5 in order to differentiate them from the $1/V_{Max}$ points. The plot includes results from Montero-Dorta & Prada (2009) (yellow inverted triangles) for comparison. Lines indicate the best fit Schechter functions. The dashed line at M_r=-16.5 is whsere surface brightness effects become important.

noted that the sSFRs in low mass galaxies may be susceptible to bias due to their low masses even if there is relatively little star formation. There is also a possibility that AGN activity may falsely bolster the star formation rates of these galaxies, though the positions of low mass galaxies on the BPT diagram imply little optical input from the AGNs (if present) to the Hα emission line fluxes.

Figure 5 indicates that galaxies with red colours in the infrared follow a similar trend in metallicity to those with bluer colours with lower mass galaxies exhibiting lower metallicities. There is some evidence for lower metallicities for the lowest mass, reddest galaxies but it is only a 3.2-σ effect.

5 DISCUSSION

5.1 Galaxy Populations as a Function of Mass

The change in slope between high and low mass galaxies in the mass and luminosity functions of red galaxies points to two separate populations of red galaxies. By mass these populations are well aligned with the red sequence (massive galaxies) and the blue cloud (low mass galaxies) as demonstrated by Blanton et al. (2005a) and Baldry et al. (2008). Morphologically the massive red galaxies have larger average Sérsic indices than the lower mass systems, but the scatter is large within individual stellar mass bins.

Starburst galaxies and AGN can both redden galaxy colours such that W1 - W2 $>$ 0.5 (Jarrett et al. 2011; Wright et al. 2010). Most (85.4%) high mass ($M/M_\odot > 10^{10}$) red (W1 - W2 $>$ 0.5) galaxies are optically classified as AGN or composites while 85.8% of low mass ($10^8 < M/M_\odot < 10^9$) red galaxies are optically classified as star-forming systems. The differences in optical classifications of red galaxies as a function of stellar mass indicates that different mechanisms may be responsible for heating the dust (only $\sim$ 13% of low mass galaxies are unclassified due to low S/N emission lines so this is not the reason for the difference).

The difference in the optical spectral properties of the high and low mass end of the red galaxy population can be interpreted in several different ways: (1) The dust heating

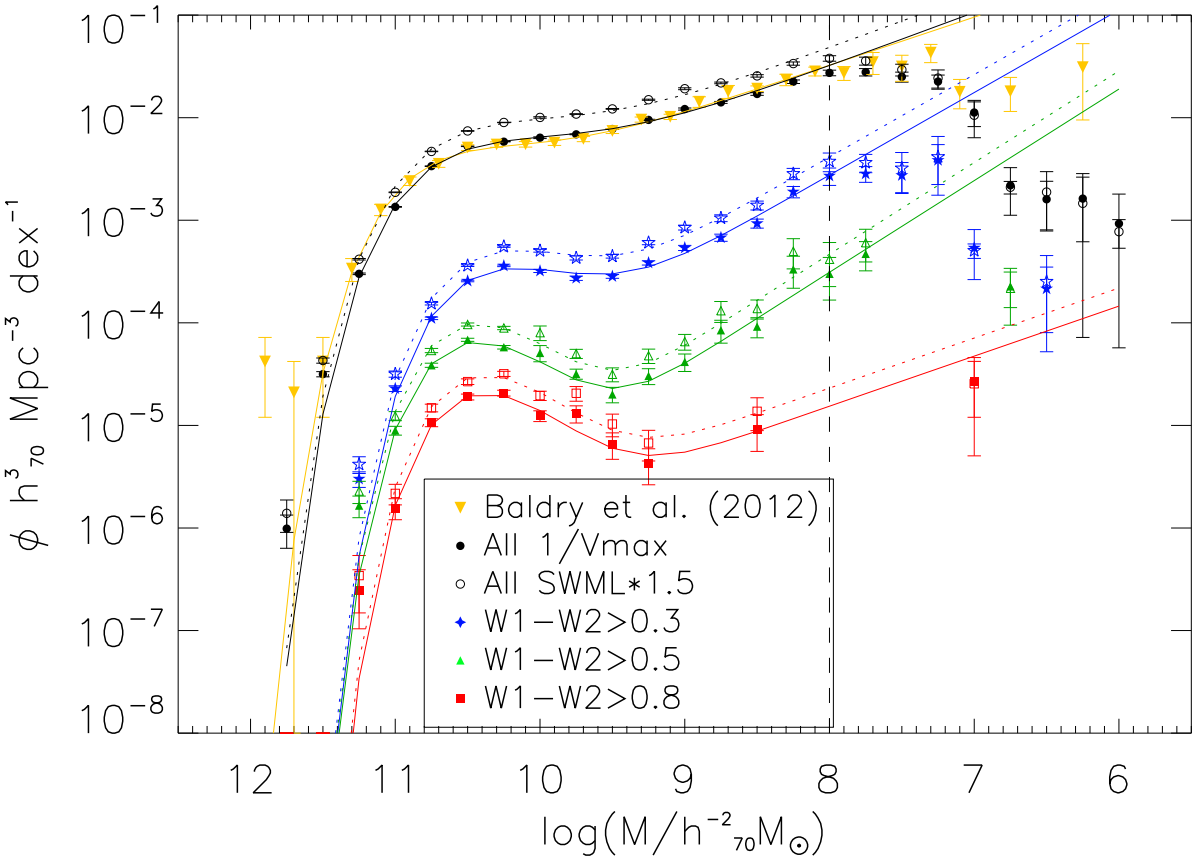

Figure 3. The number density of galaxies in our sample and W1 - W2 colour subsamples as a function of stellar mass. Filled points calculated using the $1/V_{Max}$ method and open points are calculated using our modified SWML method. SWML points and errors are shown here multiplied by 1.5 so that they may be more easily differentiable from the $1/V_{Max}$ points. Black circles were calculated using the full galaxy sample while the blue stars only include galaxies with W1 - W2 $\geq$0.3, green triangles only include galaxies with W1 - W2 $\geq$ 0.5 and red squares only include galaxies with W1 - W2 $\geq$ 0.8. Solid lines are Baldry et al. (2012)-form Schechter functions fit to the $1/V_{Max}$ points above the surface brightness incompleteness line. The dashed line at 10^8 $M_\odot$ signifies the point below which the mass function is incomplete (See Section 4). Dotted lines are our best fit Schecter functions multiplied by 1.5 so that their normalization is comparable to that of the SWML points. This figure also contains the data points and best fit Schechter function from Baldry et al. (2012) as yellow inverted triangles.

that produces the red colours is powered by different physical processes in high and low mass galaxies – AGNs at the high mass end and star formation at the low mass end; (2) the same AGNs are responsible for the dust heating over the full mass spectrum of galaxies but the AGNs are not optically visible in low mass systems due to the dusty environments; or (3) while AGNs are largely responsible for the dust heating in massive systems AGNs and/or star formation can contribute for low mass galaxies.

For the following discussion, red galaxies refers to systems with W1-W2 > 0.5. This colour cut defines the AGN region in Stern et al. (2012) and Jarrett et al. (2011) and provides better statistics than a colour cut of W1-W2 > 0.8.

5.2 Star Formation as a Driver of Dust Heating in Red Galaxies?

The simplest explanation for the differences in the optical emission line properties of high and low mass red galaxies is a difference in the physical process responsible for heating the dust. For low mass red galaxies the most likely heating mechanism is star formation.

Figure 5 shows that low mass red galaxies have higher sSFRs than their bluer counterparts while high mass red and blue galaxies have comparable sSFRs. However, there are known correlations between star formation and AGN activity so a correlation between star formation and red colours does not rule out AGNs as a power source (Netzer et al. 2007; Lutz et al. 2008; Netzer 2009; Woo et al. 2012; Rosario et al. 2012, e.g.).

One important note on stars being responsible for the red colours is that it must be the heating by young stars rather than the galaxies being red due to the stel-

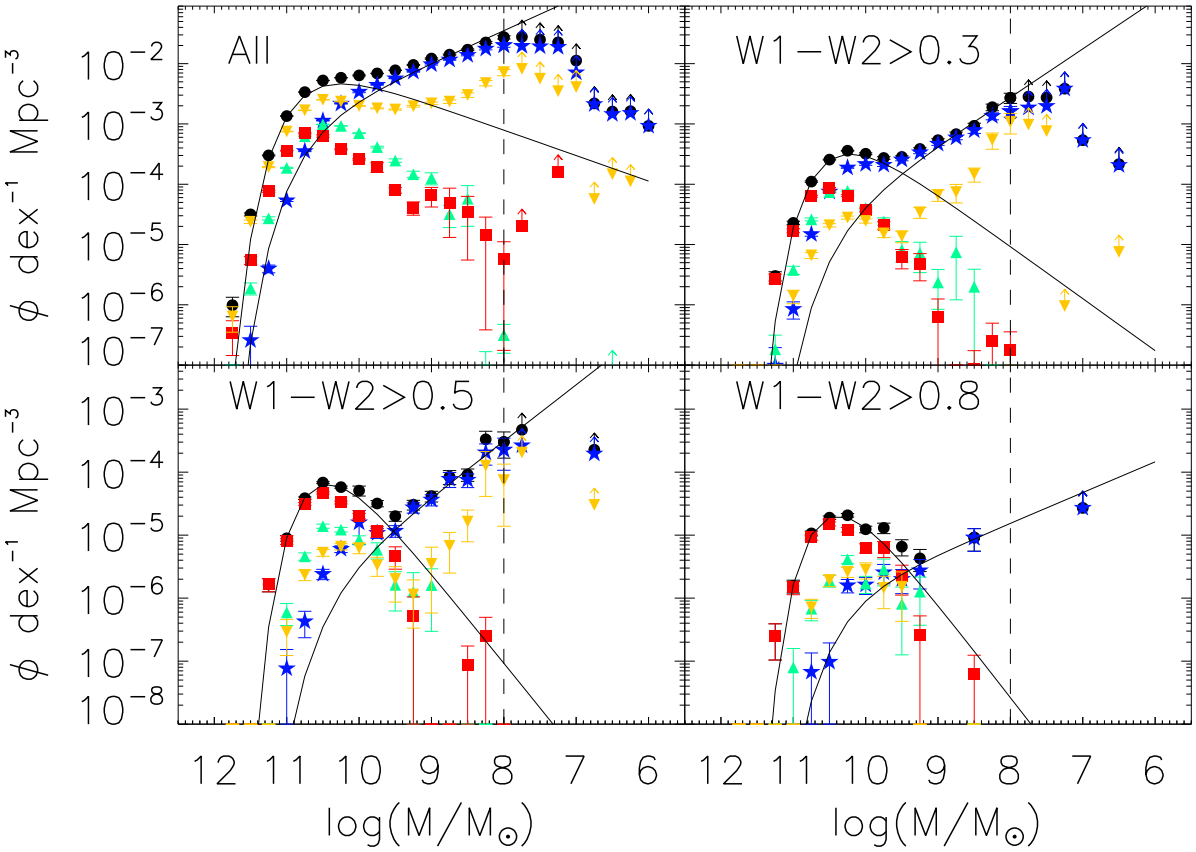

Figure 4. The $1/V_{Max}$ stellar mass function points for the full sample (top left), W1 - W2 $\geq$ 0.3 (top right), W1 - W2 $\geq$ 0.5 (bottom left) and W1 - W2 $\geq$ 0.8 (bottom right). The total stellar mass function in each colour range is shown as black circles. Optical AGNs (broad and narrow line) are shown as red squares, composite galaxies as green triangles, star-forming galaxies as blue stars and unclassified galaxies as yellow inverted triangles. The vertical dashed line is the limit below which the stellar mass function becomes uncertain due to incompleteness.

lar colours themselves because stars rarely get this red. Chen et al. (2014) observed dust-free stars in the Milky Way and found that their colours rarely exceed W1 - W2 = 0.25. Faherty et al. (2014) and Nikutta et al. (2014) provide a handful of exceptions to this rule, but the classes of stars that they observe (Wolf-Rayet and PAGB stars) are both rare and unlikely to dominate the colour of an entire galaxy. Similarly, T dwarfs and later-type stars may have W1 - W2 as high as 4.2 but are too dim to dominate the light of a galaxy (Kirkpatrick et al. 2011). Though the fraction of infrared light contribution may vary significantly from one galaxy to another, Thermally Pulsating Asymptotic Giant Branch (TP-AGB) stars' emission peaks in in the 3-4μm range and has much redder than average [3.6]-[4.5] colour (Meidt et al. 2012; Gerke & Kochanek 2013; Melbourne & Boyer 2013; Villaume et al. 2015).

While stars themselves make a negligible contribution to these red colours, Calzetti et al. (2010); Kennicutt (1998) have shown that young, hot stars can contribute significantly to dust heating through the reproccessing of UV radiation. It has also been noted that redder colours from star formation might be expected in low mass galaxies due to their lower average metallicities (Hunt et al. 2010). These lower metallicity stars produce a harder radiation field (Lee et al. 2004; Kewley et al. 2004; Moustakas et al. 2006) due to a combination of decreased mass-loss rates, higher Hayashi limits and a lack of line blanketing seen in higher metallicity stars (Levesque et al. 2010) and thus additional dust heating. However, Figure 5 shows that the metallicity of the red and blue low mass galaxies is similar so the harder radiation field in low metallicity systems is unlikely to be a key factor in which dwarf galaxies exhibit red colours.

If dust heating by star formation drives the red infrared colours, galaxies with strong, concentrated star formation (e.g., blue compact dwarf galaxies, BCDs) may be more likely to have red galaxy-wide colours. To examine this possibility, we identify the 599 galaxies in this sample classified as BCDs using the criteria of Sánchez Almeida et al. (2008). Galaxies that are identified as BCDs are more likely to also have red W1 - W2 colors. There is a 5.2 σ difference between the fraction of BCDs and all sample galaxies with W1 - W2 $>$ 0.5 and a 2.5 σ difference for galaxies with W1 - W2 $>$ 0.8. Corroborating the idea that star formation is important in driving the red colours of BCDs, those with W1 - W2 $\geq$

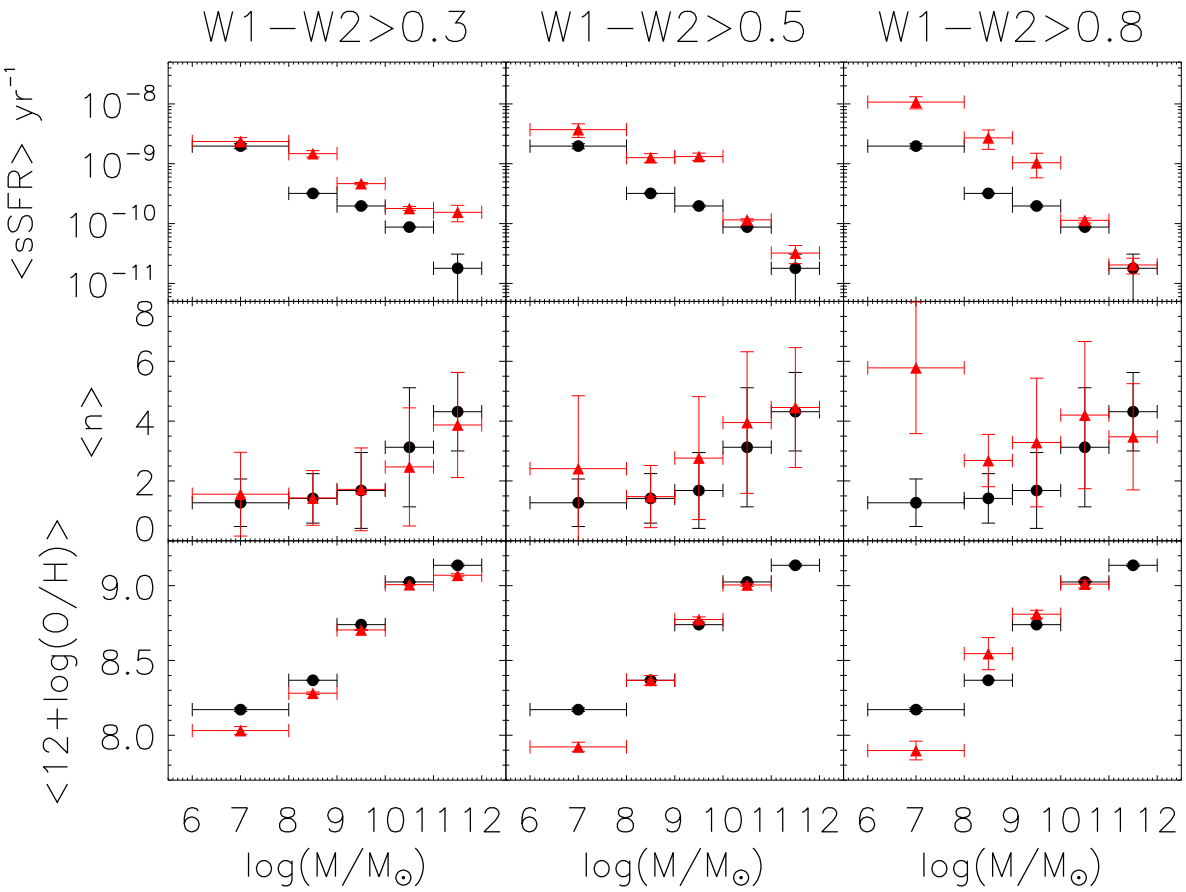

Figure 5. From top to bottom, the average specific star formation rates, Sérsic indices and metallicities of sample galaxies as functions of stellar mass and WISE colour. Black circles are the values calculated using only galaxies with W1-W2<0.3 while red triangles are calculated using galaxies with W1-W2≥0.3 (left), W1-W2≥0.5 (middle) and W1-W2≥0.8 (right). All averages are weighted using the inverse of each galaxy's V_{Max} value.

0.8 all have W2 - W3 > 4 and only 19% (7/37) with W1 - W1 ≥ 0.5 have W2 - W3 ≤ 4. 15.0% and 12.8% of galaxies with W1 - W2 > 0.5 and W1 - W2 > 0.8 in the full sample also have W2 - W3 > 4 (5.7 and 72.7 σ difference, respectively). High W2 - W3 colour is more likely to come from star formation than AGN activity because the colour comes from enhanced PAH features in the W3 band (Jarrett et al. 2013).

Given that only a small fraction of BCDs show high W1 - W2 colours (Griffith et al. 2011; Izotov et al. 2011, 2014), concentrated star formation is clearly not a sufficient condition for making low mass galaxies red. It is also possible that the red colours in these BCDs are actually powered by AGN. The spectra of 5 BCDs (out of 12) show [Ne v 3426] emission. 3 of these also show [Fe v 4227] emission (Izotov et al. 2004; Thuan & Izotov 2005; Izotov et al. 2012). Both of these high ionization lines are often associated with AGN activity and 4 out of 5 BCDs with [Ne v 3426] emission and all with [Fe v 4227] emission have W1 - W2 > 0.5 (Izotov et al. 2012).

A more detailed study of dust heating by star formation and its contribution to red colours is needed, but it is beyond the scope of this work.

5.3 AGN as the Driver of Dust Heating in Red Galaxies?

Most (85.2%) massive (10^{10} < M/M$_\odot$ < 10^{12}) red (W1 - W2 ≥ 0.8) galaxies in this sample are optical AGN or composites. However a growing number of AGNs have been identified in low mass galaxies (Barth et al. 2004; Dong et al. 2007; Greene & Ho 2007; Ghosh et al. 2008; Izotov & Thuan 2008; Jiang et al. 2011; Ho et al. 2012; Reines & Deller 2012; Schramm et al. 2013; Maksym et al. 2014; Moran et al. 2014; Satyapal et al. 2014; Yuan et al. 2014) including He2-10 (1.4×10^9M$_\odot$) (Reines et al. 2011; Reines & Deller 2012; Whalen et al. 2015), Mrk 709S (2.5×10^9M$_\odot$) (Reines et al. 2014) and SDSS J1329+3234 (2×10^8M$_\odot$) (Secrest et al. 2015). Reines et al. (2013) has found 151 optical AGNs in galaxies with $10^{8.5} < M/M_\odot < 10^{9.5}$, 0.6% of galaxies in this mass range. This fraction of low mass galaxies is similar to the 0.3% of galaxies with W1 - W2 > 0.8. However, only 2 out of 15 (13%) low mass BLAGN in Reines et al. (2013) have W1 - W2 ≥ 0.5 (1 with W1 - W2 ≥ 0.8). Inversely 11 out of 136 (8%) low mass AGNs identified with BPT line ratios have W1 - W2 ≥ 0.5 (8 have W1 - W2 ≥ 0.8) so even if the galaxies with red

WISE colours are AGNs, they are generally not the same ones that are optically classified as AGNs.

If AGNs are important for the dust heating in these low mass galaxies, almost all of them would have to be deeply embedded in dust despite these systems generally being thought to have very little dust (Cook et al. 2014; Draine et al. 2007). Akylas et al. (2012) find that 5 - 50% of AGN could be Compton-thick and still be consistent with the X-ray background, a lower percentage of the overall galaxy population than is contributed by low mass optically star-forming galaxies with W1 - W2 $\geq$ 0.5 (85%).

We have also examined the 2MASS (Skrutskie et al. 2006) colours of our sample galaxies. Only 1.6% of the full sample has J - K_s > 2, which is typical of QSOs (Warren et al. 2000; Hutchings et al. 2003) and only 168, 41 and 10 galaxies with W1 - W2 $\geq$ 0.3, 0.5 and 0.8 were matched with a 2MASS source in the AllWISE catalog. Three galaxies with 0.3 < W1 - W2 < 0.5 have J - K_s > 2, which is consistent with the 2.7$\pm$1.6 sources expected in this category. None of the galaxies with W1 - W2 > 0.5 have red 2MASS colours, but this is also statistically consistent with the 1.6% found in the full sample.

Additional observations are needed to confirm the AGN nature of low mass red W1 - W2 galaxies. X-ray observations with facilities such as *Chandra* and *XMM-Newton* have proven effective in uncovering AGN in low mass galaxies (Reines et al. 2011, 2013; Secrest et al. 2015), though as evidenced by the lack of optical emission line visibility, obscuration may be an issue. At z=0, the hard X-ray (2-10 keV) emission of an AGN with N_H=10^{24} cm^{-2} is suppressed by more than a factor of 10 (Brightman & Nandra 2011). Fortunately, the higher energy (10-195 keV) emission is reduced by a factor of less than 2 (Brightman & Nandra 2011). *NuSTAR* (Harrison et al. 2013) is capable of explaining this higher energy (3-79 keV) range and has already observed several obscured and/or low luminosity AGN (Annuar et al. 2015; Lansbury et al. 2014, 2015; Madsen et al. 2015; Ursini et al. 2015; Ricci et al. 2016).

The launch of the *James Webb Space Telescope* (Gardner et al. 2006) in 2018 will bring about the opportunity to observe the infrared spectra of low mass IR-red galaxies. Though the wavelength range of *JWST*'s NIRspec and MIRI instruments (0.6-28 μm) is shorter than that of *IRS* (5-38 μm), it will still be capable of observing spectral features such as the 6.2 μm and 11.3 μm PAH features and high ionization lines like [NeV 14.32μm] and [OIV 25.89μm] used in AGN diagnostics developed for galaxies observed with IRS (Spoon et al. 2007; Tommasin et al. 2010; Hernán-Caballero & Hatziminaoglou 2011; Magdis et al. 2013; Gruppioni et al. 2016).

5.4 Implications for Seed Black Hole Models

Two models currently exist for the origin of supermassive black hole seeds at the centres of galaxies: (1) the creation of a seed through the death of a population III star and (2) the direct collapse of a massive gas cloud Volonteri (2012, and references therein). The fraction of very low mass galaxies with central black holes (occupation fraction) can provide a test of these models, but in practice measuring the occupation fraction in low mass galaxies is difficult to do (Miller et al. 2015).

van Wassenhove et al. (2010) use these two mechanisms to seed satellites in Milky Way type haloes. The result of the van Wassenhove et al. (2010) study is that the occupation fraction is significantly lower for massive seeds than it is for the population III seeds. To compare with these models which determine the occupation fraction as a function of velocity dispersion, V-band luminosities are derived from the r-band luminosity and $g-r$ colour according to the transformations of Jester et al. (2005) and from those values velocity dispersion is derived using the V-σ relation in van Wassenhove et al. (2010).

For both models the occupation fraction at $z = 0$ is one for velocity dispersions above σ = 50 km s^{-1}. At velocity dispersion of σ <$\sim$32 km s^{-1}, which corresponds to M_r= -14.4 (just beyond the last point of the full luminosity function), the models begin to diverge with the population III seeds continuing to have an occupation fraction of one while direct collapse model seeds have an occupation fraction of 0.6. At this luminosity the fraction of optical AGN have effectively gone to zero so optical AGN would indicate either a much lower occupation fraction than predicted in either of these models or they predict a rapidly falling fraction of central black holes that are active as galaxy mass decreases.

One possible explanation for the decrease in optical AGN at lower masses is the increase in the number of AGN that are embedded in dust. Given that these are the masses at which there is a transition from early type galaxies that have small amounts of gas and dust in their ISM to late type galaxies that have significant gas and dust in their ISM, it is possible that the number of deeply embedded AGN would increase.

While it is unlikely that all low mass galaxies with red WISE colours are AGN that assumption can be used to place some constraints on the population. Galaxies with W1 - W2 $\geq$ 0.5 and W1 - W2 $\geq$ 0.8 at a luminosity of M_r $\sim$ -14.4 comprise $\sim$3% and $\sim$1% of the total number density. For the population III seed models only $\sim$3% and $\sim$1% of the black holes would, therefore, be expected to be active in these low mass galaxies because the occupation fraction is predicted to be one. For the massive seed models $\sim$5% and $\sim$2% of the galaxies would be expected to be active depending on the colour above which all of the galaxies possess embedded AGN. In both cases this still predicts a much smaller active fraction than observed in more massive galaxies (Kauffmann et al. 2003). These numbers indicate that either there is a problem with the black hole seed models or the fraction of active black holes drop with galaxy mass even if there is a substantial population of embedded AGN residing in low mass late-type galaxies. We note that mid-IR colour selection only finds AGN that dominate the bolometric luminosity of the galaxy. It is possible that there is a significant fraction of weakly accreting and optically unidentified AGNs (Satyapal et al. 2007, 2008, 2009) that would not be identified through W1 - W2 colour selection.

6 SUMMARY

We have calculated the r-band luminosity and stellar mass functions of z < 0.1 galaxies from AllWISE and SDSS DR7 for the full population, galaxies with W1 - W2 $\geq$ 0.3, W1 - W2 $\geq$ 0.5 and W1 - W2 $\geq$ 0.8. We find:

(i) Galaxies with colours redder than W1 - W2 = 0.5 make up 0.6% of the galaxy population and galaxies with W1 - W2 $\geq$ 0.8 make up 0.04% of the galaxy population for galaxy masses $10^8 < M/M_\odot < 10^9$. These are fairly rare, but not an insignificant fraction of the galaxies in the local universe.

(ii) Massive galaxies ($M/M_\odot > 10^{10}$) with colours redder than W1 - W2 $\geq$ 0.5 make up 1.0% of the galaxy population and galaxies with W1 - W2 $\geq$ 0.8 make up 0.3% of the galaxy population in that mass range. Relative to the total galaxy population massive red galaxies are also rare in the universe.

(iii) Most (85.2%) massive ($M/M_\odot > 10^{10}$) galaxies with W1 - W2 $\geq$ 0.8 are optically classified as AGN or composites, in agreement with the numbers in Stern et al. (2012) and Jarrett et al. (2013) and a good indicator that these colours are a good way to select massive galaxies with dusty AGN.

(iv) The physical mechanism responsible for the red colours in low mass galaxies is less clear than it is in their higher mass counterparts. An increase in the sSFR of red, low mass galaxies may point to star formation driving the heating. However, the possibility exists that in at least some cases the red colours are indicative of dust enshrouded AGN.

(v) Even in the unlikely case that all of the low mass red galaxies possess dust enshrouded AGN, both pop III and massive seed models indicate that the fraction of black holes that are active in low mass galaxies is significantly less than in more massive systems.

ACKNOWLEDGEMENTS

The authors would like to thank T.H. Jarrett for comments which helped improve the quality of this paper.

This study was funded by NSF grant AST-000167932.

Funding for the SDSS and SDSS-II has been provided by the Alfred P. Sloan Foundation, the Participating Institutions, the National Science Foundation, the U.S. Department of Energy, the National Aeronautics and Space Administration, the Japanese Monbukagakusho, the Max Planck Society, and the Higher Education Funding Council for England. The SDSS Web Site is http://www.sdss.org/.

The SDSS is managed by the Astrophysical Research Consortium for the Participating Institutions. The Participating Institutions are the American Museum of Natural History, Astrophysical Institute Potsdam, University of Basel, University of Cambridge, Case Western Reserve University, University of Chicago, Drexel University, Fermilab, the Institute for Advanced Study, the Japan Participation Group, Johns Hopkins University, the Joint Institute for Nuclear Astrophysics, the Kavli Institute for Particle Astrophysics and Cosmology, the Korean Scientist Group, the Chinese Academy of Sciences (LAMOST), Los Alamos National Laboratory, the Max-Planck-Institute for Astronomy (MPIA), the Max-Planck-Institute for Astrophysics (MPA), New Mexico State University, Ohio State University, University of Pittsburgh, University of Portsmouth, Princeton University, the United States Naval Observatory, and the University of Washington.

This publication makes use of data products from the Wide-field Infrared Survey Explorer, which is a joint project of the University of California, Los Angeles, and the Jet Propulsion Laboratory/California Institute of Technology, funded by the National Aeronautics and Space Administration.

This research has made use of the VizieR catalogue access tool, CDS Strasbourg, France. the original description of the VizieR service was published in A&AS 143, 23.

This research has made use of the NASA/IPAC Extragalactic Database (NED) which is operated by the Jet Propulsion Laboratory, California Institute of Technology, under contract with the National Aeronautics and Space Administration.

REFERENCES

Abazajian K. N., et al., 2009, ApJS, 182, 543
Akylas A., Georgakakis A., Georgantopoulos I., Brightman M., Nandra K., 2012, A&A, 546, A98
Alonso-Herrero A., et al., 2006, ApJ, 640, 167
Annuar A., et al., 2015, ApJ, 815, 36
Assef R. J., et al., 2010, ApJ, 713, 970
Assef R. J., et al., 2013, ApJ, 772, 26
Baldry I. K., Glazebrook K., Driver S. P., 2008, MNRAS, 388, 945
Baldry I. K., et al., 2012, MNRAS, 421, 621
Barth A. J., Ho L. C., Rutledge R. E., Sargent W. L. W., 2004, ApJ, 607, 90
Bendo G. J., et al., 2008, MNRAS, 389, 629
Blanton M. R., Roweis S., 2007, AJ, 133, 734
Blanton M. R., et al., 2005a, AJ, 129, 2562
Blanton M. R., Lupton R. H., Schlegel D. J., Strauss M. A., Brinkmann J., Fukugita M., Loveday J., 2005b, ApJ, 631, 208
Brightman M., Nandra K., 2011, MNRAS, 413, 1206
Brinchmann J., Charlot S., White S. D. M., Tremonti C., Kauffmann G., Heckman T., Brinkmann J., 2004, MNRAS, 351, 1151
Bruzual G., Charlot S., 2003, MNRAS, 344, 1000
Calzetti D., et al., 2007, ApJ, 666, 870
Calzetti D., et al., 2010, ApJ, 714, 1256
Charmandaris V., Heydari-Malayeri M., Chatzopoulos E., 2008, A&A, 487, 567
Chen B.-Q., et al., 2014, MNRAS, 443, 1192
Cook D. O., et al., 2014, MNRAS, 445, 899
Cutri R. M., et al., 2013, Technical report, Explanatory Supplement to the AllWISE Data Release Products
Dong X., et al., 2007, ApJ, 657, 700
Donley J. L., et al., 2012, ApJ, 748, 142
Draine B. T., et al., 2007, ApJ, 663, 866
Efstathiou G., Ellis R. S., Peterson B. A., 1988, MNRAS, 232, 431
Faherty J. K., Shara M. M., Zurek D., Kanarek G., Moffat A. F. J., 2014, AJ, 147, 115
Gardner J. P., et al., 2006, Space Sci. Rev., 123, 485
Geller M. J., Huchra J. P., 1989, Science, 246, 897
Gerke J. R., Kochanek C. S., 2013, ApJ, 762, 64
Ghosh H., Mathur S., Fiore F., Ferrarese L., 2008, ApJ, 687, 216
Gott III J. R., Jurić M., Schlegel D., Hoyle F., Vogeley M., Tegmark M., Bahcall N., Brinkmann J., 2005, ApJ, 624, 463
Goulding A. D., Alexander D. M., Mullaney J. R., Gelbord J. M., Hickox R. C., Ward M., Watson M. G., 2011, MNRAS, 411, 1231
Greene J. E., Ho L. C., 2007, ApJ, 667, 131
Griffith R. L., et al., 2011, ApJL, 736, L22
Gruppioni C., et al., 2016, preprint, (arXiv:1603.02818)
Harrison C. D., Colless M., Kuntschner H., Couch W. J., de Propris R., Pracy M. B., 2010, MNRAS, 409, 1455
Harrison F. A., et al., 2013, ApJ, 770, 103
Hernán-Caballero A., Hatziminaoglou E., 2011, MNRAS, 414, 500
Ho L. C., Kim M., Terashima Y., 2012, ApJL, 759, L16

Hunt L. K., Thuan T. X., Izotov Y. I., Sauvage M., 2010, ApJ, 712, 164
Hutchings J. B., Maddox N., Cutri R. M., Nelson B. O., 2003, AJ, 126, 63
Izotov Y. I., Thuan T. X., 2008, ApJ, 687, 133
Izotov Y. I., Noeske K. G., Guseva N. G., Papaderos P., Thuan T. X., Fricke K. J., 2004, A&A, 415, L27
Izotov Y. I., Guseva N. G., Fricke K. J., Henkel C., 2011, A&A, 536, L7
Izotov Y. I., Thuan T. X., Privon G., 2012, MNRAS, 427, 1229
Izotov Y. I., Guseva N. G., Fricke K. J., Henkel C., 2014, A&A, 561, A33
Jarrett T. H., et al., 2011, ApJ, 735, 112
Jarrett T. H., et al., 2013, AJ, 145, 6
Jester S., et al., 2005, AJ, 130, 873
Jiang Y.-F., Greene J. E., Ho L. C., Xiao T., Barth A. J., 2011, ApJ, 742, 68
Kauffmann G., et al., 2003, MNRAS, 341, 54
Kennicutt Jr. R. C., 1998, ARA&A, 36, 189
Kewley L. J., Dopita M. A., Sutherland R. S., Heisler C. A., Trevena J., 2001, ApJ, 556, 121
Kewley L. J., Geller M. J., Jansen R. A., 2004, AJ, 127, 2002
Kewley L. J., Groves B., Kauffmann G., Heckman T., 2006, MNRAS, 372, 961
Kirkpatrick J. D., et al., 2011, ApJS, 197, 19
Lansbury G. B., et al., 2014, ApJ, 785, 17
Lansbury G. B., et al., 2015, ApJ, 809, 115
Lee J. C., Salzer J. J., Melbourne J., 2004, ApJ, 616, 752
Lee J. C., Hwang H. S., Ko J., 2013, ApJ, 774, 62
Levesque E. M., Kewley L. J., Larson K. L., 2010, AJ, 139, 712
Loveday J., 2000, MNRAS, 312, 557
Lutz D., et al., 2008, ApJ, 684, 853
Madsen K. K., et al., 2015, ApJ, 812, 14
Magdis G. E., et al., 2013, A&A, 558, A136
Mainzer A., et al., 2011, ApJ, 731, 53
Maksym W. P., Ulmer M. P., Roth K. C., Irwin J. A., Dupke R., Ho L. C., Keel W. C., Adami C., 2014, MNRAS, 444, 866
Mateos S., et al., 2012, MNRAS, 426, 3271
Mateos S., Alonso-Herrero A., Carrera F. J., Blain A., Severgnini P., Caccianiga A., Ruiz A., 2013, MNRAS, 434, 941
Meidt S. E., et al., 2012, ApJL, 748, L30
Melbourne J., Boyer M. L., 2013, ApJ, 764, 30
Miller B. P., Gallo E., Greene J. E., Kelly B. C., Treu T., Woo J.-H., Baldassare V., 2015, ApJ, 799, 98
Montero-Dorta A. D., Prada F., 2009, MNRAS, 399, 1106
Moran E. C., Shahinyan K., Sugarman H. R., Vélez D. O., Eracleous M., 2014, AJ, 148, 136
Moustakas J., Kennicutt Jr. R. C., Tremonti C. A., 2006, ApJ, 642, 775
Netzer H., 2009, ApJ, 695, 793
Netzer H., et al., 2007, ApJ, 666, 806
Nikutta R., Hunt-Walker N., Nenkova M., Ivezić Ž., Elitzur M., 2014, MNRAS, 442, 3361
Polletta M., et al., 2007, ApJ, 663, 81
Ranalli P., Comastri A., Setti G., 2003, A&A, 399, 39
Reines A. E., Deller A. T., 2012, ApJL, 750, L24
Reines A. E., Sivakoff G. R., Johnson K. E., Brogan C. L., 2011, Nature, 470, 66
Reines A. E., Greene J. E., Geha M., 2013, ApJ, 775, 116
Reines A. E., Plotkin R. M., Russell T. D., Mezcua M., Condon J. J., Sivakoff G. R., Johnson K. E., 2014, ApJL, 787, L30
Ricci C., et al., 2016, ApJ, 820, 5
Richards G. T., et al., 2006, ApJS, 166, 470
Rosario D. J., et al., 2012, A&A, 545, A45
Rovilos E., et al., 2014, MNRAS, 438, 494
Sánchez Almeida J., Muñoz-Tuñón C., Amorín R., Aguerri J. A., Sánchez-Janssen R., Tenorio-Tagle G., 2008, ApJ, 685, 194
Satyapal S., Vega D., Heckman T., O'Halloran B., Dudik R., 2007, ApJL, 663, L9
Satyapal S., Vega D., Dudik R. P., Abel N. P., Heckman T., 2008, ApJ, 677, 926
Satyapal S., Böker T., Mcalpine W., Gliozzi M., Abel N. P., Heckman T., 2009, ApJ, 704, 439
Satyapal S., Secrest N. J., McAlpine W., Ellison S. L., Fischer J., Rosenberg J. L., 2014, ApJ, 784, 113
Schaerer D., de Koter A., 1997, A&A, 322, 598
Schlegel D. J., Finkbeiner D. P., Davis M., 1998, ApJ, 500, 525
Schmidt M., 1968, ApJ, 151, 393
Schramm M., et al., 2013, ApJ, 773, 150
Secrest N. J., et al., 2015, ApJ, 798, 38
Simard L., Mendel J. T., Patton D. R., Ellison S. L., McConnachie A. W., 2011, ApJS, 196, 11
Skrutskie M. F., et al., 2006, AJ, 131, 1163
Spoon H. W. W., Marshall J. A., Houck J. R., Elitzur M., Hao L., Armus L., Brandl B. R., Charmandaris V., 2007, ApJL, 654, L49
Stern D., et al., 2012, ApJ, 753, 30
Stern D., et al., 2014, ApJ, 794, 102
Strauss M. A., et al., 2002, AJ, 124, 1810
Thuan T. X., Izotov Y. I., 2005, ApJS, 161, 240
Tommasin S., Spinoglio L., Malkan M. A., Fazio G., 2010, ApJ, 709, 1257
Tremonti C. A., et al., 2004, ApJ, 613, 898
Ursini F., et al., 2015, MNRAS, 452, 3266
Villaume A., Conroy C., Johnson B. D., 2015, ApJ, 806, 82
Volonteri M., 2012, Science, 337, 544
Warren S. J., Hewett P. C., Foltz C. B., 2000, MNRAS, 312, 827
Whalen T. J., Hickox R. C., Reines A. E., Greene J. E., Sivakoff G. R., Johnson K. E., Alexander D. M., Goulding A. D., 2015, ApJ, 806, 37
Woo J.-H., Kim J. H., Imanishi M., Park D., 2012, AJ, 143, 49
Wright E. L., et al., 2010, AJ, 140, 1868
Xue Y. Q., et al., 2010, ApJ, 720, 368
Yan L., et al., 2013, AJ, 145, 55
Yuan W., Zhou H., Dou L., Dong X.-B., Fan X., Wang T.-G., 2014, ApJ, 782, 55
van Wassenhove S., Volonteri M., Walker M. G., Gair J. R., 2010, MNRAS, 408, 1139

This paper has been typeset from a TEX/LATEX file prepared by the author.

Table 1. Luminosity Function Schechter Parameters

Colour Range	ϕ_1^* Mpc^{-3}	ϕ_2^* Mpc^{-3}	M_r^* mag	α_1	α_2
Total	$5.659\pm0.007\times10^{-3}$	$1.949\pm0.010\times10^{-3}$	-20.753±0.013	-0.244±0.029	-1.438±0.013
W1-W2≥0.3	$4.323\pm0.159\times10^{-4}$	$9.795\pm1.121\times10^{-5}$	-19.985±0.035	0.463±0.078	-1.682±0.034
W1-W2≥0.5	$7.150\pm0.362\times10^{-5}$	$4.929\pm1.422\times10^{-6}$	-20.354±0.066	0.473±0.129	-1.911±0.084
W1-W2≥0.8	$2.385\pm0.154\times10^{-5}$	$5.782\pm6.766\times10^{-7}$	-20.378±0.128	0.217±0.226	-1.973±0.351

Note. — Blanton et al. (2005a)-form Schechter functions fit to our data as described in Section 3.

Table 2. Stellar Mass Function Schechter Parameters

Colour Range	ϕ_1^* Mpc^{-3}	ϕ_2^* Mpc^{-3}	$\log(M^*/M_\odot)$ $\log(M_\odot)$	α_1	α_2
Total	$4.407\pm0.004\times10^{-3}$	$5.833\pm0.545\times10^{-4}$	10.620±0.005	-0.557±0.024	-1.524±0.018
W1-W2≥0.3	$3.733\pm0.066\times10^{-4}$	$1.757\pm0.408\times10^{-5}$	10.281±0.015	-0.137±0.064	-1.804±0.057
W1-W2≥0.5	$7.095\pm0.315\times10^{-5}$	$1.256\pm0.595\times10^{-6}$	10.280±0.025	0.423±0.123	-1.892±0.124
W1-W2≥0.8	$2.178\pm0.211\times10^{-5}$	$5.593\pm7.798\times10^{-7}$	10.216±0.043	0.479±0.224	-1.487±0.397

Note. — Baldry et al. (2012)-form Schechter functions fit to our data as described in Section 3.